Chemical Engineering Journal 452 (2023) 138587

Contents lists available at ScienceDirect

Chemical Engineering Journal

journal homepage: www.elsevier.com/locate/cej

Ultra-fast and low-cost electroactive biochar production for electroactive-constructed wetland applications: A circular concept for plant biomass utilization

Yamini Mittal [a,b], Pratiksha Srivastava [c], Naresh Kumar [d], Manish Kumar [a,b], Saroj Kumar Singh [a,b], Fernando Martinez [e], Asheesh Kumar Yadav [a,b,e,*]

[a] CSIR-Institute of Minerals and Materials Technology, Bhubaneswar, Odisha, 751013, India
[b] Academy of Scientific and Innovative Research (AcSIR), Ghaziabad, Uttar Pradesh, 201002, India
[c] Biotechnological Processes Unit, IMDEA Energy, Avda. Ramón de la Sagra 3, 28935, Móstoles, Madrid, Spain
[d] Soil Chemistry and Chemical Soil Quality Group, Wageningen University, 6708 PB Wageningen, The Netherlands
[e] Department of Chemical and Environmental Technology, Rey Juan Carlos University, Mostoles, 28933, Spain

ARTICLE INFO

Keywords:
Circular bioeconomy
Electroactive constructed wetlands
Plasma biochar
Kiln biochar
Constructed wetland coupled microbial fuel cell
Bioelectricity generation
Pollutant removal efficiency

ABSTRACT

This study demonstrates two sustainable processes to produce electroactive biochars and their application in electroactive constructed wetlands (CWs) for providing a circular route for biomass utilization and technology up-gradation for wastewater treatment along with electricity generation. With the use of *Canna indica* biomass generated in CWs operation, the current study produced two different biochars that differ in their physico-(electro)chemical properties related to the preparation method used. This study used plasma based processing to produce ultrafast biochar (PB) within a few minutes resulting in more crystalline biochar with high electrical conductivity compared to the amorphous biochar material produced by using the drum kiln processed biochar (KB) method. These biochars were used in developing electroactive constructed wetlands coupled with microbial fuel cells (CW-MFC) and were operated in batch mode together with commercial granular graphite (GG) substrate-based CW-MFC as control. PB was developed from high-temperature plasma processing in 6.0 min, whereas KB was prepared in bulk amount from semi-controlled combustion process in kiln method and took 3–4 days before final biochar preparation. Electrical conductivity (EC) of the biochar and GG material were found to be in the order of PB > GG > KB, indicating PB as a highly conductive material that assisted in microbial electron transfer. Accordingly, the highest current and power densities of 628 mA m^{-3} and 126 mW m^{-3}, respectively, were also achieved with PB. The COD removal of 72.42 ± 2.61 %,72.32 ± 2.98 % and 59.91 ± 3.21 % was found in CW-MFC-GG, CW-MFC-KB and CW-MFC-PB microcosms, respectively.

1. Introduction

Water resources are being subjected to continuous degradation due to population growth, agricultural and urban expansion, changes in land use, and over-exploitation by virtue of economic development [1,2]. Though there have been significant advances in technological development in the field of wastewater treatment, more often, the issue is of high energy consumption and hence, operating costs hinder their field success. Thus, there is a growing need to develop more environmentally responsible wastewater treatment technologies with balanced environmental, economic, and societal sustainability. This led to a shift in focus towards nature-based sustainable technologies that are low cost, eco-friendly, and leave low environmental footprints [3].

In present times, sustainability-oriented concepts *i.e.*, circular use of resources are being strongly advocated aimed at transforming the current linear fossil fuel-based economy towards a cost-effective and waste recycling-based economy made on utilization of renewable sources [4]. For low-cost and sustainable wastewater treatment, natural treatment systems especially like CWs can play a key role through wastewater treatment, nutrient recovery, and useful plant biomass production [5,6]. Besides these, potential application of biomass based materials and their application in wastewater treatment have gained attention of researchers focusing towards circularity development in recent times [7].

Considering this, in 2010, a novel integrated technology, *i.e.*,

* Corresponding author at: CSIR- Institute of Minerals and Materials Technology, Acharya Vihar, Bhubaneswar, Odisha, 751013, India.
E-mail addresses: asheesh@immt.res.in, asheesh.yadav@gmail.com (A.K. Yadav).

https://doi.org/10.1016/j.cej.2022.138587

Available online 11 August 2022

integration of constructed wetlands (CWs) and microbial fuel cell (MFCs) (henceforth referred as CW-MFCs) has been developed and introduced by Yadav et al. [8] for wastewater treatment with the additional benefit of bioelectricity generation. Integrated CW-MFCs resolve some of the challenges faced by these technologies individually, such as high land area requirement and slow treatment rates in CWs, and low oxygen reduction rate, up-scaling issue in MFC technology [9,10]. Over time, CW-MFC have been assessed and optimized in several design aspects such as electrode surface area, electrodes distance optimization, electrode number, electrode material, electron transfer mechanism, separators, system configuration, functional aspects such as operational conditions (flow direction, aeration), flow type (batch or continuous), and performance aspects such as different wastewater treatment, greenhouses gas emission reduction, *etc.* [2,11]. All these optimizations were aimed towards enhanced removal of pollutants and nutrients, improving energy output, and new application development [2]. However, still, CW-MFC faces energy losses and often ends up exhibiting low power output than expected with the scope of the pollutant removal efficiency enhancement. In MFCs or microbial electrochemical technology (MET), electrode materials play a crucial role in terms of microbial colonization, microbial electron transfer, electron holding capacity, charge transfer resistance (R_{ct}), solution resistance (R_s) and thus impacting the overall performance of CW-MFCs [12–14]. Among these, a fundamental parameter, *i.e.,* rapid microbial colonization is supported by high surface area, microporosity, and rough surface morphology of electrode material [13,14]. Granular activated carbon (GAC) and granular graphite (GG) have been widely utilized as substrate achieving maximum power density generation of 880 mW m^{-3} and 321 mW m^{-3}, respectively [3]. A recent study observed highest chemical oxygen demand (COD) and nitrate removal (86.7 % and 87.1 %, respectively) with smallest filler size resulting from higher surface area available and wider diversity in microorganisms species, whereas, enhanced bioelectricity generation was observed with large filler size owing to abundance of electrochemically active bacteria (EABs) [14]. Dewatered alum sludge (DAS) has been proposed as a promising substrate in CW-MFC studies due to its tendency for pH elevation and thus, allowing enhanced electricity generation and high P adsorption affinity permitting good PO_4^{3-}-P removal [15,16]. DAS as a substrate displayed power density generation in the range of 7.9 to as high as 1413.2 mW m^{-2} in different lab studies [17,18]. Lately, pyrrhotite ($Fe_{1-x}S$; $0 < x$ less than 0.125) and alum sludge was introduced as substrate in two-tiered CW-MFCs [19]. The results revealed 80–87 % of ammonium removal, facilitation of efficient electron transfer, and current production by high conductive pyrrhotite, co-occurrence of feammox and pyrrhotite based autotrophic denitrification. Thus, suggesting that the more conductive is the substrate, higher are the chances of electron transfer and presence of exoelectrogens (EABs), which ultimately lead to accelerate oxidation and reduction reactions at anode and cathode, respectively. However, still, only few substrates have been tested in CW-MFC studies, including commonly GAC, GG, DAS, quartz, zeolite, and pyrrhotite.

Biochar has recently emerged as one of the potential materials in environmental remediation studies attributed to its highly porous and stable nature, although its application in CW-MFC technology has been very limited so far (see supplementary information). In 2019, the anode electrode of CW-MFC based on nZVI amended biochar was found conducive to bioelectricity generation and organic compound degradation [20]. Recently, Sonu et al. [21] reported the use of corn cob biochar as media/substrate in CW-MFC for treatment of real textile wastewater attaining higher power density up to 23.8 mW m^{-2}, and higher COD removal, and decolorization efficiency, 17 %, and 25 %, respectively, in comparison to CW-MFC without corn cob biochar. Nevertheless, most of the works are done only to utilize adsorption properties due to high surface area or functional groups. Electron exchange properties to enhance microbial reaction kinetics are rarely covered (see supplementary information). There are still need for developing and testing a novel method for preparation of biochars with electron conductive properties. Besides, physico-chemical properties of biochars synthesised from different processes, process time, mass scale production for large scale application, are some of the issues in using biochars in CWs, which are yet to be explored.

Thus, in the present research work, two innovative and sustainable ways of preparing biochars were used and the prepared biochars were applied as substrate in CW-MFCs. This work providing a conceptual and mechanistic understanding of biochar production methods and their consequent physico-(electro)chemical applications in environmental systems. Further, this work is designed to demonstrate the uses of conductive biochar for developing next-generation constructed wetlands (*i.e.,* CW-MFC). These methods and their implication in efficiency have not been reported in the literature and add significant value to the current knowledge of the application and efficiency of biochar in environmental application.

These biochars were derived from the plant biomass waste of *Canna indica,* a water-loving macrophyte, harvested from an operational CW facility located inside CSIR-IMMT, India. Thus, overall representing the idea of circularity through utilization and implementation of synthesized biochar in CW-MFCs with harvested biomass from the CWs. Herein, we used a high-temperature plasma synthesized biochar *viz.* plasma biochar (PB), with a generation time of 6 min, as one of the conductive electrode substrates in CW-MFCs. Whereas, the second biochar was prepared through the drum kiln method in a semi- controlled combustion environment *viz.* kiln biochar (KB), which requires a total preparation time of 3–4 days, including quenching, drying, and sieving. To the best of our knowledge, this is the first study implementing plasma biochar and kiln biochar as sustainable conductive substrates in CW-MFC systems.

2. Material and methods

2.1. Material preparation

Canna indica biomass was harvested from field scale CW facility of CSIR-IMMT, Bhubaneswar, India. Harvested biomass was consisting mainly leaves and stem portions. Harvested biomass was sun dried for two weeks and stored. Prior to converting this biomass to biochar, sun dried biomass was first washed with tap water several times to remove dirt and then immersed in 5 % H_2SO_4 overnight for cleaning to remove any calcitrant surface sorbed ions, organics, or atmospheric deposits to avoid further contamination of biochar and to ensure the biochar only comes from plant biomass. Later, H_2SO_4 immersed biomass was washed with tap water again multiple times and left for a week for drying. Thereafter, biomass was chopped into small pieces (5–7 cm) with a cutter and used as raw material for two different types of biochar formation *i.e.*, plasma biochar (PB) and kiln biochar (KB). In addition to synthesis of PB and KB, a commonly utilized conductive substrate *i.e.,* granular graphite (GG) of 2–4 mm diameter was also commercially purchased and used as substrate in CW-MFC microcosm fabrication.

2.2. Biochar preparation

2.2.1. Plasma biochar (PB) preparation

A single-step conversion of dried biomass of *Canna indica* into thermal plasma processing was carried out in indigenous pot type DC extended arc thermal plasma reactor. The detailed design of the plasma reactor is reported by Singh et al. [22]. Briefly, the reactor is comprised of two graphite electrodes arranged in vertical position, where the cathode is placed on top, and a bottom graphite crucible (15 cm height and 10 cm diameter) works as an anode and hearth of the reactor. The cathode remains in contact with the inside base of the graphite crucible, as shown in Fig. 1(a).

For biochar making, dried biomass of *Canna indica* is filled in the crucible and covered with a lid. The biochar making was carried out in batch mode and typical gas flow conditions comprised of an argon flow

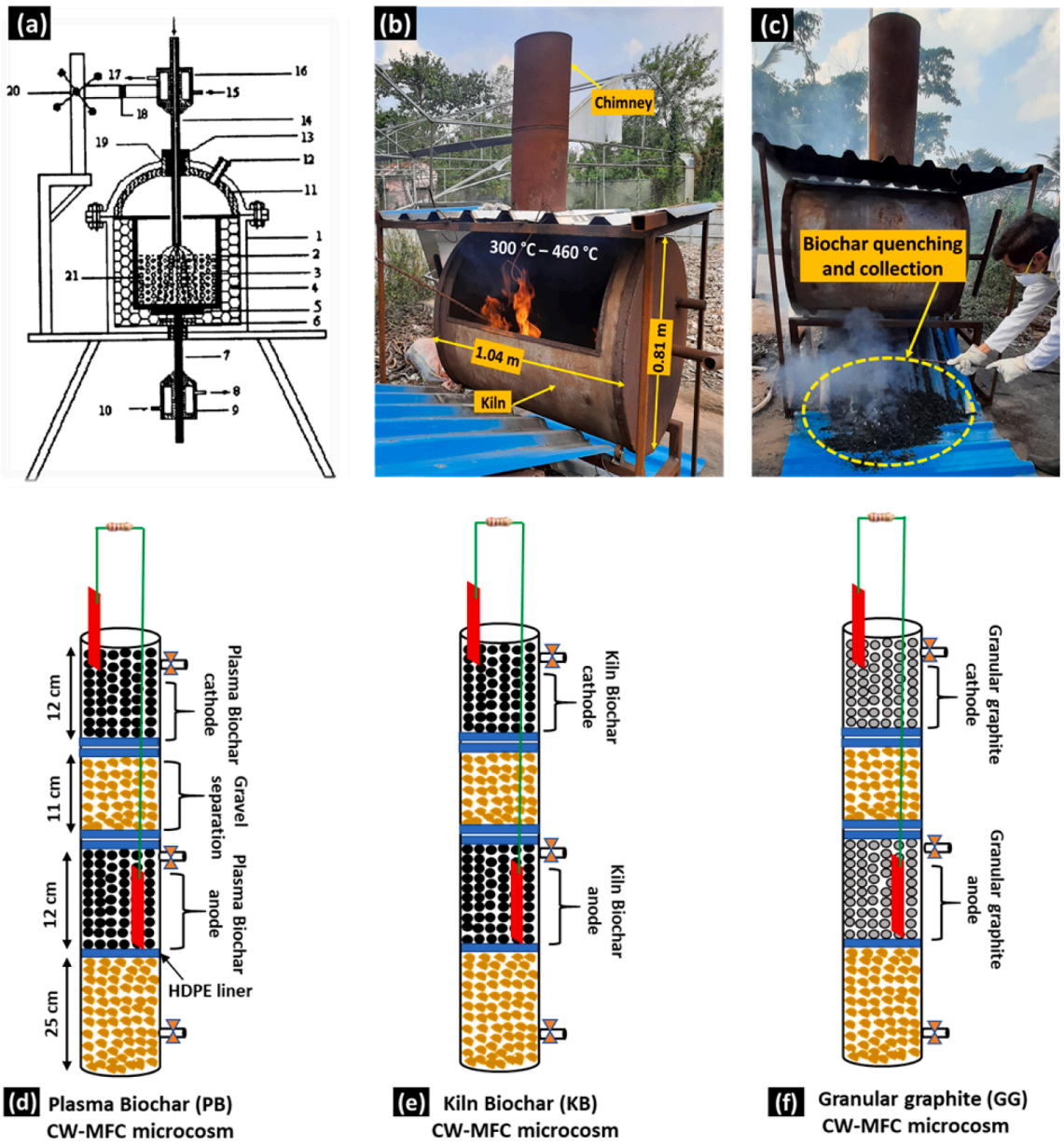

Fig. 1. (a) Schematic view of plasma reactor as described in Singh et al. [22], where 1. Casing; 2. Crucible of graphite; 3. Plasma; 4. Alumina bubble; 5. graphite base; 6. Alumina bush; 7. Bottom graphite electrode; 8. Water outlet; 9. Copper connector; 10. Water inlet; 11. Magnesia lining; 12. Exhaust; 13. graphite bush; 14. Top graphite electrode; 15. Water inlet; 16. Copper connector; 17. Water outlet; 18. Electrical insulation; 19. Alumina bush; 20. Pinion and rack and 21. Charge., (b) Rotatable drum kiln (c) quenching and collection of biochar prepared, schematic diagram of (d) PB based CW-MFC microcosm, (e) KB based CW-MFC microcosm, and (f) GG based CW-MFC microcosm.

rate of 2 L min^{-1}, voltage load of 50.0 V, and arc current of 300 A. After argon was employed for plasma generation, both N_2 and O_2 gas were also passed. Further, at the end of the biochar preparation, graphite crucible was allowed to cool down to room temperature.

The plasma processing time was just 6.0 min. Altogether, 31.0 g of PB was prepared from 247.0 g of dried *Canna indica* biomass. An Infrared Pyrometer (Mikron, model: M90 - *R*3, USA) was used for the measurement of temperature inside the graphite crucible.

2.2.2. *Preparation of drum kiln biochar (KB)*

A semi-closed rotatable drum kiln was developed in CSIR-IMMT, Bhubaneswar by Paul S. Anderson during his visit (Fig. 1(b)). Details of the rotatable drum kiln is available elsewhere [23]. Briefly, a rotatable drum kiln consists of a rotatable semi-closed drum equipped with a vent (chimney), as shown in Fig. 1(b). The kiln ensures the semi-controlled combustion of biomass in the limited presence of oxygen and allows bulk biochar preparation with a single run. For the preparation of biochar, dried *Canna indica* biomass was fed inside the kiln. This biomass was ignited using a matchstick and left for around 5 min. Then it was covered with a lid for limiting the presence of air. Biomass was charred for approximately 25–30 min. Afterward, charring was stopped by quenching with tap water to prevent the complete burning of biomass to ash, as shown in Fig. 1(c).

The temperature of biomass charring inside the kiln was recorded several times at different points with the help of an Infrared thermometer (59 Max + IR thermometer, FLUKE, USA). The recorded temperature ranged between 300 °C and 460 °C during the whole process of biochar preparation.

Subsequently, wet biochar was dried in the oven at 80 °C for two days and then sieved (Ø 600 μm) to get fine powdered biochar. Overall,

3.816 kg of dried *Canna indica* biomass resulted in 791.2 g of dried and sieved KB.

2.3. Physical adsorption study

Adsorption capacity of PB, KB and GG for ammonium and phosphate was evaluated. A standard aqueous solution of 40 mg L^{-1} ammonium prepared using NH_4Cl salt (AR grade, Hi media Pvt. ltd., India) and 20 mg L^{-1} phosphate solution prepared using KH_2PO_4 salt (AR grade, Hi media Pvt. ltd., India) in double distilled water. Adsorption experiments were carried out in triplicate, for this, 1.0 g of PB, GG and KB were added to 80 mL of each ammonium and phosphate solution in conical flasks. The conical flasks were placed to an orbital shaker (Spinix Orbital shaker MC-02, Tarson) and run it at 130 rpm. Thereafter, an aliquot was taken at various time periods (10, 20, 30, 40, 50, 60, 70 min) and analysed for residual aqueous ammonium and phosphate concentration to know the adsorptive removal of these ions.

2.4. Experimental setup

Three CW-MFC microcosms were fabricated with 3 different filter materials *viz.* PB, KB, and GG as shown in Fig. 1 (d), (e), and (f). All microcosms was fabricated in a poly vinyl chloride (PVC) pipe with dimensions of 60.0 cm × 2.5 cm (height × diameter) and were equipped with three identical ports at 3.5 cm, 29.0 cm and 56.5 cm from the top. At first, all 3 microcosms were filled with calcareous gravel (5–8 mm Φ) till 25 cm from the bottom, and then a 12.0 cm layer of specific filter material *i.e.,* KB, GG and PB was added to bring up to a height of total 37.0 cm which is functioning as anode. This portion of every microcosm was embedded with a graphite plate anode charge collector of 19.6 cm^2. Further, anode and cathode portions were separated by 11 cm of calcareous gravel layer *via* a layer of High-density Polyethylene (HDPE) liner which has four small holes of 2.0–3.0 mm each for percolating the wastewater at both ends as shown in Fig. 1 (d), (e) and (f). This HDPE arrangement was made for acting as a dissolved oxygen diffusion barrier between upper cathode and lower anode zones. Above this separation, a 12 cm of the cathode was made with respective filter material and embedded with graphite plate cathode charge dispenser (area-19.625 cm^2) similar to anode. However, a part of the (1.5 cm) cathode charge dispenser was placed above the water level as suggested by Yang et al. [24] to promote oxygen rich environment at cathode. Anode and cathode charge collector/dispenser were connected with insulated copper wire and the exposed area was sealed and insulated with epoxy. The other free ends of anode and cathode charge collectors/dispenser were connected with a resistance.

2.5. Inoculation, experiment start-up and operation

Microcosms were inoculated with the sludge of a previously functioning CW-MFC microcosm in the CSIR-IMMT laboratory. Initially, 50 % v/v of inoculum was fed in dilution with synthetic wastewater (with 0.25 g L^{-1} glucose as carbon source) to each microcosm. Synthetic wastewater also contained 0.111 g L^{-1} $NaHCO_3$, 0.0445 g L^{-1} KH_2PO_4, 0.0371 g L^{-1} $MgCl_2{\cdot}6H_2O$, 0.0842 g L^{-1} $(NH_4)_2Fe(SO_4)_2{\cdot}6H_2O$, 0.0301 g L^{-1} $CaCl_2{\cdot}2H_2O$, 0.1119 g L^{-1} $(NH_4)_2SO_4$ and 1 mL L^{-1} trace metal mix constituted of 0.222 g L^{-1} $ZnSO_4{\cdot}7H_2O$, 0.39 g L^{-1} $Na_2Mo_4{\cdot}2H_2O$, 2.86 g L^{-1} H_3BO_3, 1.81 g L^{-1} $MnCl_2{\cdot}4H_2O$, 0.079 g L^{-1} $CuSO_4{\cdot}5H_2O$ and 0.05 g L^{-1} $CoCl_2$ adopted from Villasenor et al. [25]. All the chemicals used in the study were acquired from Hi-Media Pvt. ltd. The theoretical carbon and ammonium concentration in the synthetic wastewater were calculated as 266.7 mg L^{-1} and 37 mg L^{-1}, respectively.

All the experiments were performed in batch mode at an room temperature of 29 ± 2 °C with three days of hydraulic retention time (HRT)/contact time. At first, the inoculum was distributed evenly to all microcosm, and for about the first 20 days, microcosms were run in full recirculation mode followed by 50 days of 50:50 recirculation mode, *i.e.,* freshly prepared synthetic wastewater was mixed with 50 % of effluent on a daily basis. Further, samples were collected including influent samples on the day of filling and effluent after three days of HRT from each microcosm. Refilling of microcosms with influent was carried out with the help of a peristaltic pump from the lower most port.

2.6. Chemical and electrochemical analysis

Samples were filtered using Whatman grade 1 (Whatman, USA) filter paper before analysis. COD, ammonium, phosphate and nitrate concentrations were analyzed as described in standard methods of American Public Health association (APHA) [26]. Dissolved oxygen (DO) and oxidation–reduction potential (ORP) measurements were carried out by Hach meter (HQ40D, USA), and solution pH was measured using pH 1500, EUTECH instrument. The voltage was recorded with handheld (FLUKE 178, USA) digital multimeter on a daily basis. The percentage removal of COD, NH_4^+, NO_3^- for PB, GG, and KB microcosms was calculated by Eq.1.

$$\%\ removal = \frac{Infulent\ concentration - effluent\ concentration}{influent\ concentration} \times 100 \quad (1)$$

Polarization study of PB, GG, and KB microcosms was carried out after reaching a steady-state performance, by varying external resistance from 90 MΩ to 1 Ω using a resistor box (Model 1040, Time electronics). Each resistance was retained for 15 min. before the recording of voltage. Electrochemical parameters were calculated using standard by V = I × R (ohm's law), P = V × I, and thereafter, the polarization curve was drawn between voltage (V), current density (mA m^{-3}), and power density (mW m^{-3}). Where, anodic zone volume (in m^3) of the microcosms was considered while calculating current density and power density.

Calculation of coulombic efficiency (CE) was carried out for batch experiment with the following equation adopted from Liu et al. [27]. Where CE refers to the number of electrons recovered as electric current with respect to theoretical coulombs generated from complete oxidation of organic content and can be calculated by Eq. (2).

$$CE(\%) = \frac{Fb\Delta Sv}{M} \times 100 \quad (2)$$

In Eq. 2, F is the Faraday constant (*i.e.,* 96,485C mol^{-1} e^-), b represents the number of electrons transferred per mol of O_2 (*i.e.*, 4 mol e^- mol^{-1} O_2), M is molecular mass of oxygen (*i.e.,* 32 g O_2 mol^{-1} O_2), v is the volume of microcosm in L and ΔS is a change in COD between influent and effluent (g L^{-1}).

Bio-electrochemical behavior of PB microcosm during electricity generation was studied by cyclic voltammetry (CV) (Model- 660 E, CHI, electrochemical workstation, USA). CV was carried out in a two-electrode mode, where one electrode acts as the working electrode and the other as both reference and counter electrode in a fused mode as described previously [28]. CV was performed at a low scan rate of 10 mV s^{-1} over the potential range of −0.95 mV to 0.6 mV against anode of the microcosm as working electrode and cathode as counter electrode fused with a reference electrode. Additionally, with the help of an impedance analyzer (IM 3570, Hioki, Japan), the conductivity of PB, KB, and GG were calculated by powdering PB, KB, and GG followed by compressing into disks through a pelletizer (M−30, Techno search Instruments, Hydraulic press, India). Further, conductivity was calculated through the following Eq. (3):

$$Conductivity(\sigma) = \frac{L}{AR} \quad (3)$$

Where L represents the thickness of pellet in cm, A is the area of pellet cm^2, and R is resistance through pellet in Ω.

2.7. Antimicrobial study

A confirmatory test was also performed to examine if the use of PB

and KB resulted in any antimicrobial activity. Tests were performed in triplicates using outlet wastewater from PB and KB microcosms. In addition, the antimicrobial activity of PB and KB was also tested with *S. aureus* (*Staphylococcus aureus*; gram-positive) and *E. coli* (*Escherichia coli*; gram negative) for confirmation and controls were setup using Ciprofloxacin antibiotic. At first, nutrient agar (NA) was prepared by mixing 13 g NA (Hi media Pvt. ltd.) with 500 mL milli-Q water in cotton plugged conical flask. Then, sterilization of NA along with petri dishes, cotton swabs and pipette tips was carried out in autoclave (model 9AVV-4, Smita Scientific, India) for 20 min at 140 °C. Afterward, NA was left to cool down and later poured into Petri dishes inside laminar air flow (model HPsafe- 1200LC, Heal Force, China) and left overnight for solidification. Day after, samples of PB and KB microcosm, *E. coli* and *S. aureus* were spread in petri dishes using the swabbing method (10^9

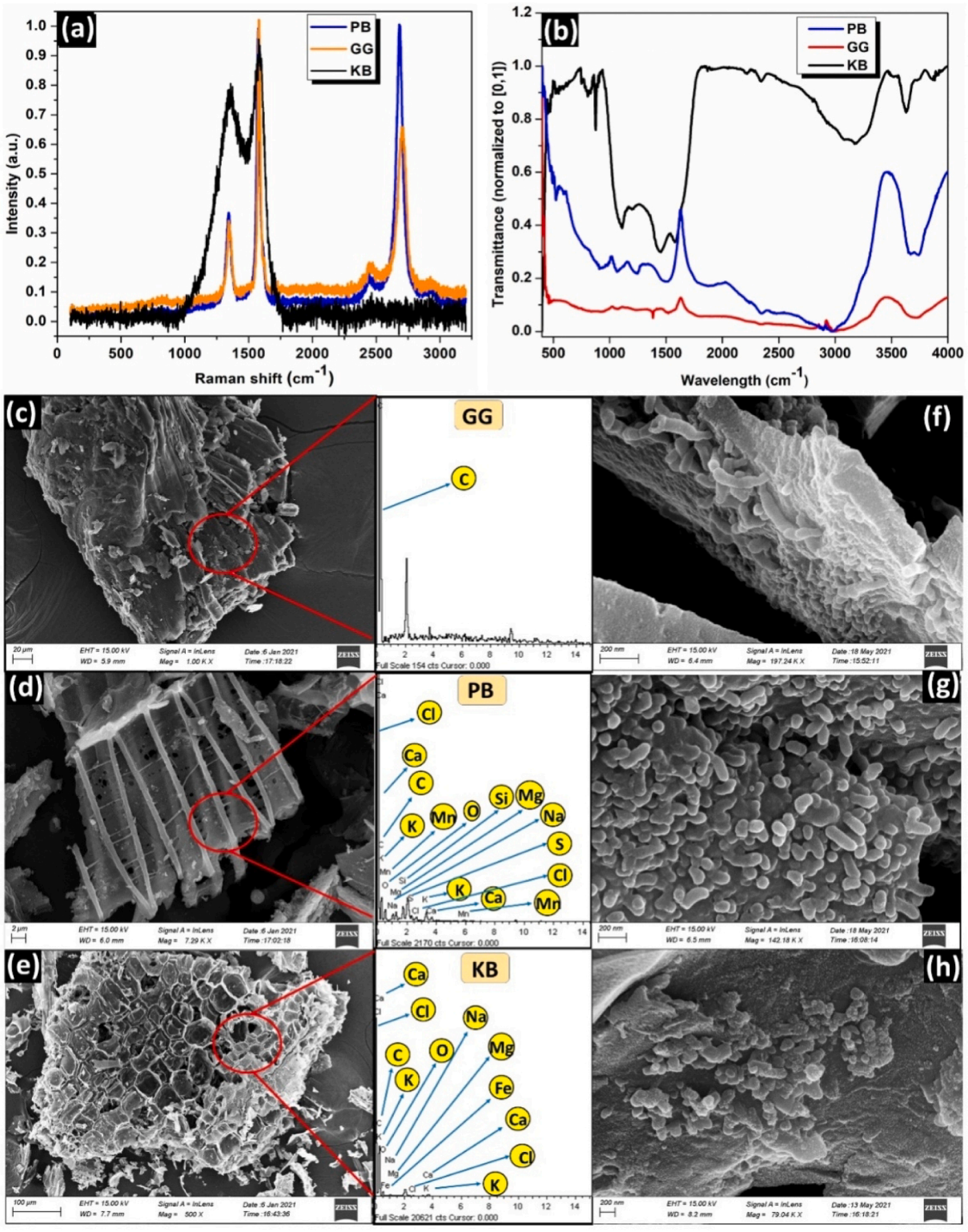

Fig. 2. (a) Normalized Raman spectra, (b) FTIR spectrum of GG, PB and KB and SEM - EDX spectra of raw untreated (c) GG, (d) PB, (e) KB and SEM micrograph of CW-MFC treated (f) GG, (g) PB and (h) KB.

cells). Since both biochar samples were of solid nature, biochar was kept in the center of the petri dish as per spot inoculation method, whereas, inoculation with 50 μL of 5 % w/v antibiotic Ciprofloxacin was carried out with well diffusion method. All the prepared petri dishes were covered with a lid and kept in an incubator at 37 °C for 24 h for microbial growth. The next day, every petri dish was observed under laminar air flow for any kind of inhibition zones and measured in case of appearance of any inhibition zones.

2.8. Characterization techniques

Physical and chemical characterizations were performed on ground PB, KB and GG samples. Raman spectroscopy was carried out using with Ar-Kr ion laser of 514 nm wavelength (Renishaw, UK). Field emission scanning electron microscopy with energy dispersive X-ray (FESEM-EDX) was executed through Zeiss Supra 40, Oxford Instruments, Germany. Fourier transform infrared spectroscopy (FTIR) was carried out by spectrum GX, Perkin Elmer, USA. Brunauer–Emmett–Teller (BET) surface area was determined from adsorption-desorption nitrogen isotherms after degassing samples at 120 °C in ASAP-2020 equipment (Micromeritics, USA). Elemental composition data was obtained using a Unique-plus High-Performance Elemental Analyser, model 0400.201011, Germany. Ash content determination was done by heating PB and KB samples at 650 °C in muffle furnace for 6 h. Ash content was calculated as the percentage residue remaining after organic matter removal by muffle furnace. Further, oxygen content was determined by the following Eq. (4) adopted from Enders et al. [29].

$$O\left(\%\frac{w}{w}\right) = 100 - ash\left(\%\frac{w}{w}\right) - C\left(\%\frac{w}{w}\right) - H\left(\%\frac{w}{w}\right) - N\left(\%\frac{w}{w}\right) \quad (4)$$

3. Results and discussion

3.1. Biochar characterization

Raman spectra of KB, GG and PB is shown in Fig. 2 (a). The occurrence of peaks in the range of 1340–1350 cm^{-1} and 1570–1590 cm^{-1} represents the D and G bands, respectively. D and G bands correspond to structural defects vibrations of sp^2 carbon and in-plane vibrations of sp^2 bonded graphitic carbon structure, respectively [30]. Generally, the ratio of the intensity of I_D/I_G exemplifies: i) distorted degree, ii) crystallographic structure, and iii) sp^2 domains size of graphite structure in the material. In the present study, both PB and GG showed I_D/I_G ratio of $\approx$ 0.357, whereas KB had a ratio of 0.867. These results indicated the amorphous nature of KB and reduced sp^2 domains in KB carbon structure, whereas PB ratio indicated its crystalline nature and increased sp^2 domains of graphite structure [30]. Raman spectra of KB exhibited very broad peaks (Fig. 2 (a)), and this behavior is basically owing to the presence of amorphous carbon structures in a high proportion [31]. Whereas sharp peaks of Raman spectra in the case of PB is attributed to the crystalline carbon form. In Fig. 2 (a), D band of PB is more intense than GG, suggesting that PB achieved defect-induced conductivity. The strong Raman band between 2500 and 2800 cm^{-1} corresponds to a completely ordered 3D graphite structure [32]. This band basically corresponds to the overtone of D band and is therefore also called as 2D or D*. The occurrence of graphite structure in PB is called turbostratic crystallites, a 2D order emerging from parallelly ordered carbon structure planes. Apart from other amorphous structures, these turbostratic sheets resist volumetric shrinking and thus this unequal shrinking leads to formation of micropores and microcracks resulting in increased surface area. Contrarily, in KB, a broad peak is observed between 2500 and 2800 cm^{-1} which signifies distorted 3D packing/structure than GG. The appearance of a peak at 2950 cm^{-1} in both PB and GG is induced by disorder, and it is associated with the D + G combination mode [32]. Moreover, the results in this study are consistent with Kercher and Nagle [33], reporting the conversion of disordered carbon present in lignocellulosic biomass to atomically more ordered carbon structure at temperatures > 400 °C and then further increase in temperature *i.e.*, > 700 °C led to increase in crystallinity. The relatively modest growth of ordered carbon structure in KB was presumably due to low pyrolysis temperature of 400–500 °C [34]. Conclusively, from Raman spectra, it can be deduced that PB has attained much higher defect-induced conductivity as compared to KB and can be considered as a more conductive packaging substrate for CW-MFC fabrication.

Fig. 2 (c), (d), and (e), depicts the surface morphology of GG, PB, and KB by FE-SEM images and elemental composition using EDX. Fig. 2 (c), shows a SEM image of raw GG with stacked sheet-like structure and its corresponding EDX shows only the presence of carbon, suggesting pure graphite with no impurity. This SEM morphology is in agreement with simple graphite powder observed previously [35]. Further, in Fig. 2 (d) and 2 (e), PB depicts sheet-like structure, whereas KB displayed a honeycomb-like structure. The sheet-like morphology of PB and GG corroborates the observation of a strong 2D band because of the layered structure as ascertained in the Raman spectra. This porous nature of both biochars may enhance biofilm attachment affinity and growth in comparison to GG [36]. Several studies have stated that biochars derived from the botanical origin exhibits the archetypal cellular structure of the parent feedstock material, which significantly contributes to providing bulk macroporosity to the biochar [37,38]. Further, these macropores could act as channels for smaller micropores, thus increasing overall surface area, facilitating adsorption of organic molecules and aiding wastewater treatment [37]. Through SEM visualization, PB and KB may provide high surface area owing to their porous, groove, and sheet-like structure as compared to GG. EDX analysis revealed the presence of several metal ions in low amounts such as Na, Mg, K, Ca, Mn, and nonmetallic elements Si, S, Cl in PB samples, while KB contained metal ions like Na, Mg, K, Ca, Fe and only Cl as a nonmetallic ion. Both PB and KB contained the highest atomic % weight of C element *i.e.,* 59.06 % and 73.87 %, respectively, hence confirming the formation of biochar. The presence of other metallic and nonmetallic ions could be owing to uptake of these ions by *Canna indica* plants. A similar finding of elements in EDX has also been reported previously for biochar from *Canna indica* at different temperatures [39]. These metal ions could play an important role in contaminants adsorption through inner-sphere complexation or co-precipitation, but also the presence of metal ions could provide a notion of facilitating electron transfer mechanism, although it might not be happening according to results noted by Sun et al. [34]. Immobilized metals contained in the pyrogenic carbon were not responsible for electron transfer owing to distinct reduction potentials of surface quinones and mineral metals. Also, electrons were found to be stored in graphene-like sheets of biochar and rapidly released with the availability of electron acceptors stating the geocapacitor mechanism [34]. In addition to this, the electron holding capacitance of biochar is said to increase with the increase in generation temperature [34], implying high electron holding capacitance in PB. Conclusively, from FESEM and Raman spectroscopy it can be inferred that PB is more conductive whereas KB is less conductive in nature; however, both depict some extent of porosity, whereas graphite is found to be less porous.

Nitrogen adsorption–desorption isotherms were conducted to determine specific BET surface area, macroporosity, microporosity, and pore volume. BET measurements revealed the specific surface area in the order of PB > KB > GG as 15.74 > 5.00 > 2.44 $m^2\ g^{-1}$. Micropore volume also followed the same order sequence as 0.006250 > 0.002661 > 0.002488 $cm^3\ g^{-1}$, respectively. Consequently, validating the highest surface area and porosity in plasma generated biochar. A high surface area of PB could lead to enhanced microbial attachment, whereas substantial porosity might increase substrate availability to the innermost biofilm, increasing overall power density generation. This could be explained by the accessibility of large pores by microbial adhesion, while small micropores contribute to the conductivity enhancement by virtue of increased surface area for extracellular electron transfer by

exoelectrogens [37].

In order to further evaluate microbial cell attachment to PB, KB, and GG, microcosms treated fraction was studied by SEM and compared with raw untreated PB, KB, and GG in Fig. 2 (f), (g), and (h). The SEM micrograph of PB shows more microbial cell density compared to KB and GG. Besides, these SEM images also confirm the biochar-supported microbial colonization in both PB and KB samples. High cell density in PB may imply more electron transfer and thus might improve the overall efficiency of PB based CW-MFC in comparison to KB and GG based CW-MFC microcosms.

The biochar yield was 20.73 % and 12.55 % for KB and PB, respectively, indicating a decrease in yield with the increase of temperature. CHNS analysis revealed an increase in the C content from 46.69 % (KB) to 78.84 % (PB) with the increase in biochar production temperature, as shown in Table 1. Whereas H and O content decreases with an increase in temperature, thus resulting in the decrease of H/C and O/C ratios (Table 1). These results suggested that with the rise in temperature, the produced biochar has a more aromatic structure and less hydrophilic surface. This is consistent with previously reported studies [39], and results of polar functional groups by FTIR. Also, the low ash content in PB showed high carbon content as compared to KB, which may be due to the hindrance of aromatic C forms by high ash content [29].

Physical adsorption study revealed the highest ammonium and phosphate removal in PB of 29.67 % and 94.94 %, respectively. In contrast, KB and GG depicted phosphate removal of 9.51 % and 9.05 % and ammonium removal of 26.19 % and 1.00 %, respectively. Results revealed that all the materials in our experiment showed saturation in ammonium and phosphate removal in less than 70 min and exhibited no further removal through adsorption. This implies that some of the phosphate and ammonium removal in these experiments was a result of adsorption, suggesting that removal will be high at the initial stage of microcosm operation and will reach saturation soon after. The observed removal by PB, KB, and GG could be explained with FTIR spectra as shown in Fig. 2 (b).

In Fig. 2 (b), FTIR results revealed a decrease in the total functional groups with an increase in the applied temperature [40]. This could be due to volatilization, polymerization, and mineralization processes during the plasma processing of biochar, as reported previously [41,42]. Red shift has been noted with PB compared to KB, as shown in Fig. 2 (b). Aromatic C—H bending vibration shifted to 913 cm^{-1} in the case of PB with the formation of the new broad peak at 1497 cm^{-1} attributed to increased C═C vibrations with diminishing of peak occurring at 1584 cm^{-1} (C═O) in comparison to KB. Thus, suggesting a decrease in the polar functional group with an increase in pyrolysis temperature [42]. The formation of a new peak at 1064 cm^{-1} and 1239 cm^{-1} in PB can be ascribed to the skeletal mode of C—C and C—O bonds and epoxy group C—O—C vibrations, respectively [43]. In the FTIR spectrum of graphite, no significant peak for relevant functional groups was observed, but the appearance of weak bands was noted. Few weak bands could also be resulting from exfoliated graphite process; for instance, a peak occurring at 1382 cm^{-1} corresponds to nitric acid (HNO_3) from graphite exfoliation [43]. A weak band at 1534 cm^{-1} may be due to C═O vibration, and a band appearing between 3000 and 4000 cm^{-1} could be assigned to adsorbed water molecules [42,43].

The highest phosphate adsorption was noted in PB, which is in agreement with previous studies, where, an increase in biochar formation temperature led to decreased functional groups exhibiting an increase in phosphate adsorption capacity, possibly related to metal ion precipitation reaction between phosphate and biochar calcium and magnesium [40,42,44]. Whereas, both biochars exhibited nearly the same amount of ammonium removal, which corroborates with the study stating ammonium removal is not influenced by biochar surface area [40]. Besides, the ammonium removal in PB is not as high as phosphate removal due to loss of polar groups in PB with an increase in temperature [45]. Studies also have speculated the positive relationship between biochar acid functional groups and ammonium adsorption [40]. In the case of GG, as revealed by SEM and BET surface area data, GG has the least porosity and surface area, thus showing minimal ammonium and phosphate removal by adsorption.

3.2. Antibacterial study

In order to ensure the viability of using PB and KB for microcosm fabrication, the antimicrobial test was carried out. With both the biochars, substantial microbial growth was observed with no appearance of any visibly apparent inhibition zone as shown in Fig. 3 (a), (b), and (e), (f). Also, no inhibition zone was observed with *E. coli* and *S. aureus* cultures, suggesting that biochar did not show any inhibitory effect for bacterial growth. In addition, in Fig. 3 (a), (b), (c), (e), (f), and (g), significant growth of microbes can be observed surrounding spot inoculated biochar, suggesting biochar could be acting as a support matrix for microbe adherence and growth. Similar results were previously reported, where biochar was assumed to be a biocarrier for the growth of microbes in bioreactors owing to its specific surface area and porous structure [46,47]. Fig. 3 (i) and (j), shows a control experiment which was performed to: i) ensure that appeared growth in previous plates are only driven by microbes, since microbes exhibit inhibition zone and ii) give information about the existence of any resistant microbial colony. In the present study, Fig. 3 (i) and (j) showed inhibition zone formation of 5.2 cm and 6.6 cm in 50 μL well-diffused ciprofloxacin with microbes of PB and KB microcosm wastewater, respectively. It can also be noted that one type of bacterial colony is resistant to antibiotics, and the occurrence of spot growth in plates is attributed to microbes of PB and KB microcosm wastewater. Fig. 3 (k) and (l) are controlled to ensure that Ciprofloxacin, *E. coli,* and *S. aureus* bacteria are capable of carrying out their functions and not degraded or reached their death phase. Wherein, 7 cm and 5.6 cm of inhibition zone were counted with *E. coli and S. aureus*, respectively.

3.3. DO, pH and ORP profile of microcosms

DO, pH, and ORP profiling are the crucial parameters to comprehend the environmental condition inside the microcosms. ORP of the system indicates the potential for aerobic or anaerobic microbial metabolism inside the microcosm medium. In the same way, pH and dissolved oxygen can detail about possible nature of microbial activity present inside the system [48,49]. ORP and DO monitoring can distinguish the anaerobic and aerobic conditions in the microcosms [48]. The average DO values in upper (U) and lower (L) regions of microcosms were 4.94 ± 0.90 mg L^{-1}, 1.35 ± 0.28 mg L^{-1}; 1.60 ± 0.57 mg L^{-1}, 1.47 ± 0.315 mg L^{-1}; 6.10 ± 1.04 mg L^{-1}, 1.83 ± 0.54 mg L^{-1} in PB, GG and KB, respectively (shown in Fig. 4 (a)). DO concentrations in the lower region of the

Table 1
Physicochemical properties of GG, PB, and KB (*Canna indica* waste-derived biochar).

Sample	Ash content (%)	Elemental content (%)				Atomic ratio		BET surface area	Micropore volume	Electrical Conductivity
		N	C	H	O	H/C	O/C	$m^2 g^{-1}$	$cm^3 g^{-1}$	μS cm^{-1}
PB	17.5	0.33	78.84	0.318	3.012	0.0040	0.0382	15.74	0.006250	58914.695
GG	0	0.01	95.52	0.326	4.144	0.0034	0.0433	2.44	0.002661	14169.468
KB	24.05	2.22	46.69	2.577	24.46	0.0551	0.5239	5	0.002488	3.17534

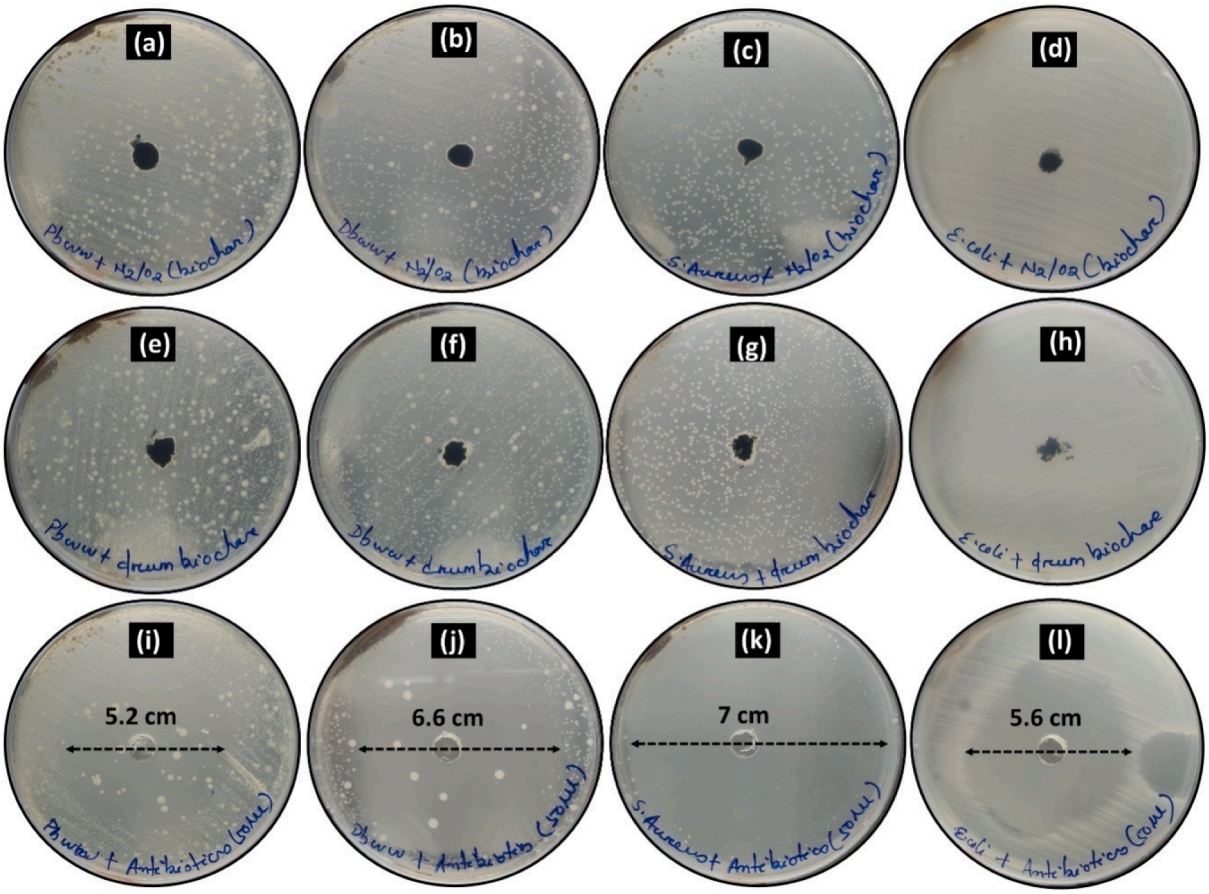

Fig. 3. Illustrates the antimicrobial activity of PB and KB with (a) and (e) PB microcosm wastewater, (b) and (f) KB microcosm wastewater, (c) and (g) *S. aureus* and (d) and (h) *E. coli*, respectively *via* spot inoculation method. The antimicrobial effect of ciprofloxacin on PB microcosm wastewater, KB microcosm wastewater, *S. aureus* and *E. coli* are represented by (i), (j), (k) and (l), respectively *via* well diffusion methodology.

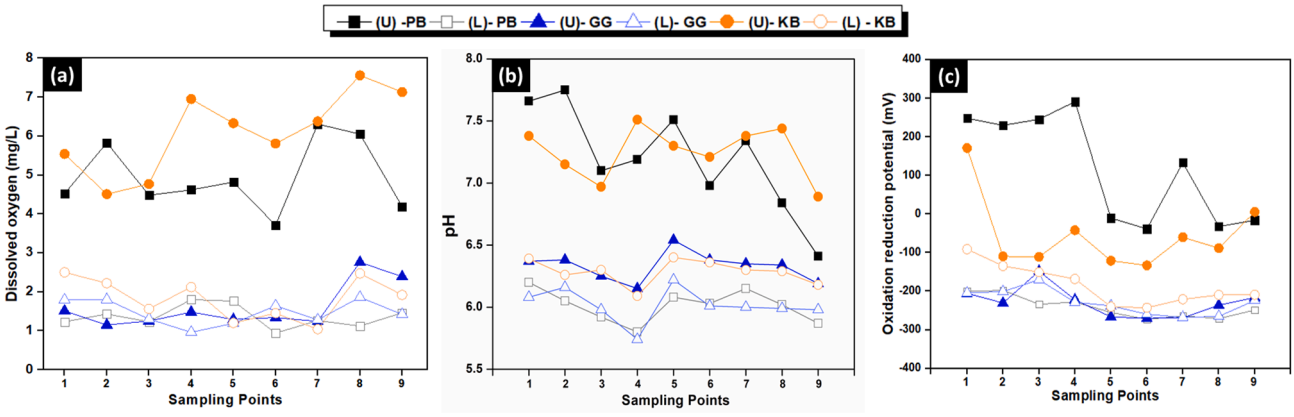

Fig. 4. (a) Dissolved oxygen, (b) pH, and (c) oxidation–reduction profile of PB, GG, and KB microcosms.

microcosm were lower in comparison to the upper region, owing to DO consumption in the lower region and O_2 diffusion from the atmosphere in the upper region. High oxygen diffusion in the upper region was observed in both biochar substrate microcosms, which may be further correlated with a drop in the water level resulting from: i) high water holding capacity of biochar and ii) longer batch operation of microcosm for 3 days of HRT. Drop in the water level creates void space filled with air which enhances the air diffusion in microcosm till deeper level and raises the DO level. The drop-in water level was recorded on 1st, 2^{nd,} and 3rd day as PB (1.5, 2.2, 3 cm), GG (0.3, 0.6, 1.4 cm) , and KB (2.3, 3.4, 4.95 cm) , respectively. Results revealed water level dip order from highest to lowest as KB > PB > GG, wherein for GG, no significant drop was observed. Water level drop order is also in agreement with DO data, where DO level increases with an increase in the water level drop in microcosm. Whereas the DO level in the lower region was found in the same range for all the microcosm and also the measured DO levels lie in the desirable range for microbial activity (*i.e.,* 0.5–2 mg L^{-1}) and functioning of EABs [50,51]. However, in the case of GG microcosm, no distinct DO separation was observed in the lower and upper regions. Less segregated DO levels were also noted by Srivastava et al. [52] in the

range of 1.8–2.5 mg L^{-1} in the upper region and 0.16–0.56 mg L^{-1} in the lower region involving granular graphite as an anode as well as cathode material for subsurface flow CW-MFC.

pH levels in microcosm were measured in the lower and upper region of microcosms with PB (7.19 ± 0.42, 6.01 ± 0.12), GG (6.32 ± 0.11, 6.01 ± 0.13), and KB (7.24 ± 0.21, 6.28 ± 0.10) as shown in Fig. 4 (b). With these observations, the microcosms configuration allowed the neutralization of the anolyte and the catholyte and thus preventing undesirable pH gradient between anode and cathode, thereby restricting electrode potential loss. As a result, it shall not limit the current generation [53]. pH data also reveals analytes of all microcosms were not acidified, preventing any decrease in microbial activity and not affecting electron transfer performance at the anode [54]. Upper region pH is always found slightly higher than lower due to proton generation in the lower region with oxidation of glucose and consumption of protons in the cathodic region for reduction reactions. However, no significant demarcation was observed in the case of GG microcosm, which might be due to adequate buffering capacity of the CW-MFC system, however, at the same time, low oxygen availability at cathode further limits the rise of pH at cathode by restricting proton consumption [58]. A similar pH distribution range was observed in other CW-MFC studies employing granular graphite as packaging substrate [2,49]. In the case of PB and KB microcosms, upper region pH was noted near circumneutral and slightly differed in comparison to the lower region. This could be due to: i) sufficient amount of oxygen diffusion in biochar microcosm, resulting in high cathodic reduction rate and thus consumption of protons and raising the pH value and ii) acid-neutralizing capacity of the biochar could have raised the pH to circumneutral value [55].

Furthermore, variation in ORP values was recorded with an increase in time of microcosm operation, except for the case of GG microcosm, where ORP in the upper and lower region were −229.3 ± 38.81 and −228.57 ± 32.92, respectively. These results are in agreement with Srivastava et al. [52], where only a minor difference in ORP value near the surface in comparison to bottom water was recorded with granular graphite substrate. In the case of PB microcosm (shown in Fig. 4 (c)), up to 4 months of microcosm operation, high positive ORP values were observed *i.e.,* 253.58 ± 26.27 mV in the upper zone. However, after 4 months of operation, ORP values decreased *i.e.,* measuring −10.5 to 133.2 mV in range as shown in Fig. 4 (c), suggesting a reduced environment. Throughout the PB microcosm operation, ORP values of the lower region were found stable as −241.13 ± 28.36 mV. However, high variation in the upper zone signifies alterations in the electroactivity in the medium with time. The positive ORP values near the surface signify aerobic conditions, whereas the negative values at the bottom describe anaerobic conditions [48]. The generation of the electronegative environment in the upper region of the PB microcosm after four months could be due to the slow rate of proton movement from the anodic region to the cathodic region, or it may correlate with organic matter oxidation rate in the PB microcosm [56].

Furthermore, for KB microcosm ORP in the upper region varied from −133 mV to + 170.9 mV, and for the bottom region, it varied in the range of −90.9 mV to −242.8 mV. In Fig. 4 (c), it can be visualized that the ORP value of the bottom region gradually decreased to a more negative value with a longer operation time of KB microcosm and further stabilized to nearly < -200 mV. The greater the difference between upper and lower region ORP, the higher will be the gradient of potential difference, promoting the higher flow of electrons from anode to cathode and thus enhanced electricity generation [50,51]. Considering the above fact, PB has the highest difference in upper and lower ORP values followed by KB and least in GG; thus, there will be a higher flow of electrons which should be reflected in terms of electricity generation and enhanced pollutant removal.

3.4. Electrochemical studies

Based on the results of electric conductivity (EC) as shown in Table 1, EC of PB is many times greater than KB and 4.15 times greater than GG. The increased electrical conductivity of carbon material is generally the consequence of high treatment temperature [57]. As the *Canna indica* feedstock processed through high temperature, volatilization of organic matter occurs, which gradually results in the rise of graphite structure. Wherein, breakage of C—H bonds leads to loss of insulating matter, and generation of a more ordered form of carbon structure contributes to the increment of EC [58]. These EC results are also in agreement with the observation of Yu et al. [59], where EC improved by increasing the charring temperature of biochar above 600 °C, produced from rice straw. Several studies reported that high EC acted as an additional benefit by decreasing the internal resistance of the MFC systems and even assisting faster cathodic reaction in soil bio-electrochemical systems [13,60]. Thus, on the basis of EC data, the PB material was found to be highly conductive in nature even more than GG, and accordingly, electrochemical studies of PB microcosm were further elaborated in detail.

Cyclic voltammetry (CV) is an electroanalytical technique that measures potential differences across the redox activities of the system and interface of both components and solution bound to bacteria in bio-electrochemical systems. During metabolic activities in the microcosms, protons and electrons are being generated and simultaneously consumed. So when an external voltage is applied, there is a generation of potential difference inside the microcosm against which electrons start moving towards the anode and get deposited, giving a CV voltammogram [61]. CV of PB microcosm at the start of the experiment and after six months of experimentation has been shown in Fig. 5 (a). Both oxidation, and reduction phenomena can be observed here, indicating reversible nature. Reversible oxidation and reduction of any component is annotated by a peak on both lower and upper curves [62,63]. In the present study, peaks of CV may correspond to excreted redox mediators and cellular components owing to mixed bacterial suspension [63]. From Fig. 5 (a), an increase in the current value after six months of microcosm operation can be observed compared to the start of the experiment. The increased current value signifies an increase in electrocatalytic biofilm activity owing to either: i) rising cell density at the electrode surface or ii) individual cell possessing rise in the count of membrane-bound electron transfer proteins [64]. The occurrence of peaks can be attributed to redox signals of mediators such as NADH/NAD^+ and FADH/FAD^+. Wherein, peak at −0.3 V may be related to redox mediators NAD^+/NADH which have the ability to reduce protons and thus suggest strong reducing phase in the PB microcosm [62]. Moreover, NAD^+/NADH are also able to redirect the increased intracellular electrons to the anode [65]. However, the same peak diminishes after 6 months of microcosm operation, suggesting a weakening of proton reduction reactions. Even then, due to high EC of PB, it could serve as the cell to cell conduit between electron-donating and electron-accepting cells promoting direct interspecies electron transfer (DIET) [12]. A shift of redox signals to lower potentials can be observed in the CV of PB microcosm after six months compared to the start of the experiment. This potentially could be due to the growth of PB microcosm biofilm under limited electron acceptor conditions which shifted the redox peaks to lower potentials and indicating limited substrate oxidation [66]. Also, with time, the surface of biochar may be covered with contaminants or microbes, leading to hindrance in further colonization of microbes and thus limiting substrate oxidation.

3.5. Electricity generation

The voltage output was recorded for the entire duration of this study for PB, KB, and GG microcosm, as shown in Fig. 5 (b). A continuous increase in voltage output was observed from day 1 to day 3 of HRT, and the highest voltage output for every microcosm was found to be on the 3^{rd} day of HRT. This indicates: i) continuous oxidation of glucose by the microcosm biofilm and ii) high leftover glucose concentration in every microcosm even on 3^{rd} day. At the start of the experiment, the open

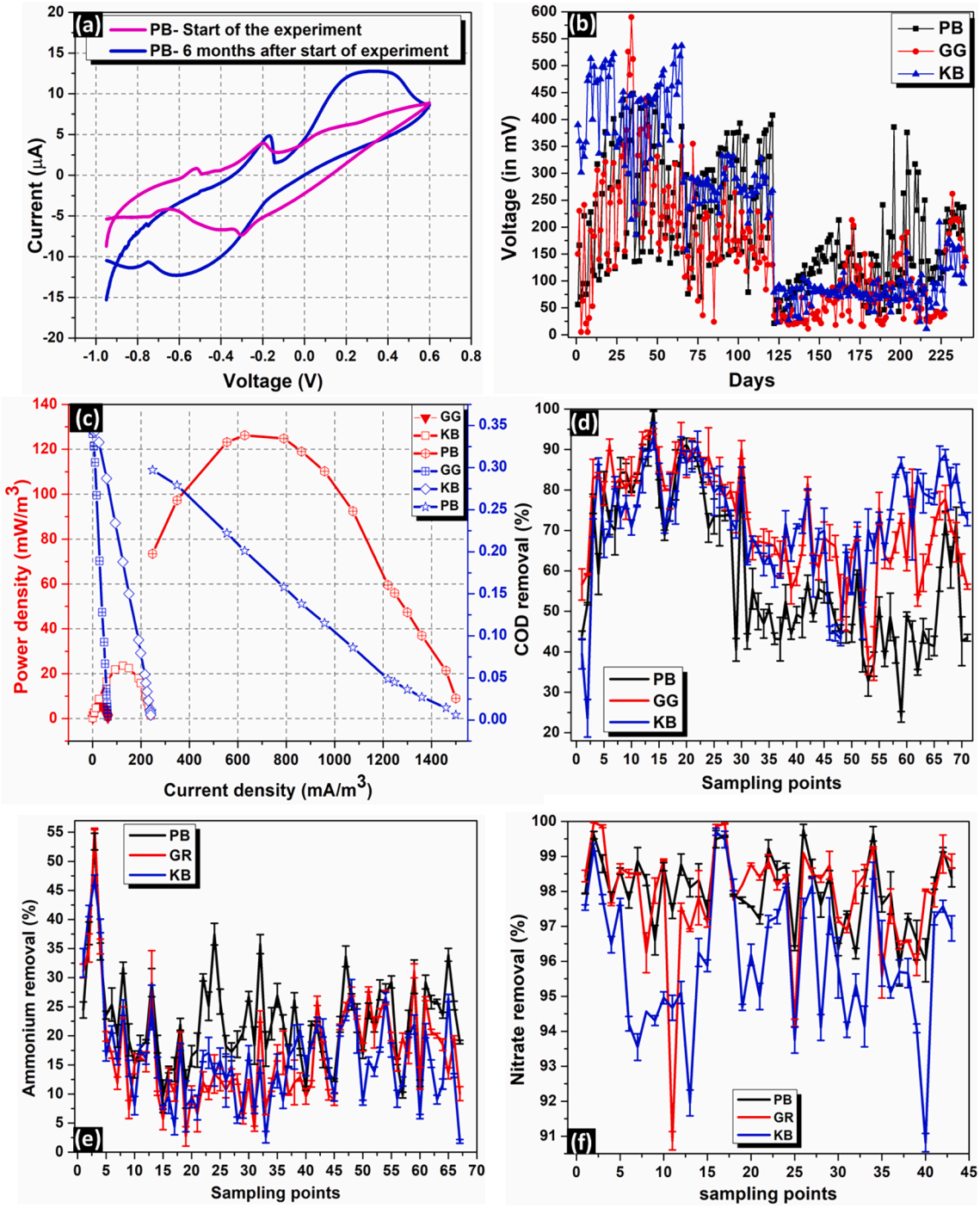

Fig. 5. (a) CV voltammogram of PB microcosm at the start of experiment and after 6 months, (b) voltage generation, (c) polarization curve, (d) percentage COD removal, (e) percentage ammonium removal and (f) percentage nitrate removal by PB, GG and KB microcosms.

circuit's highest voltage output was achieved in the GG microcosm, followed by KB and PB of 590, 537, and 461 mV, respectively. However, after polarization, highest voltage was achieved in PB microcosm of 408 mV. Besides, the drop in voltage profile after 120 days in Fig. 5 (b) refers to the event of connecting specific external resistances after polarization. Furthermore, to estimate the internal resistance of PB, GG, and KB, polarization current was plotted relating voltage, current density and power density as shown in Fig. 5 (c). The highest current density and power density can be observed in the PB microcosm of 628.12 mA m^{-3} and 126.25 mW m^{-3}, respectively. Whereas, for KB and GG, the values for current density and power density were recorded as 125.33 mA m^{-3}, 23.56 mW m^{-3}, 29.07 mA m^{-3} and 5.495 mW m^{-3}, respectively. Despite high EC of GG, one reason for low power density and current density in KB and GG microcosms can be high internal resistance occurred due to ohmic losses inside the system. Besides, it was also reported that amorphous forms of carbon generated at low temperature incur both high internal resistance and act as barriers which limit electron transfer and thus reduces electricity generation [34].

The difference in power densities can also be attributed to the variation in materials surface area, porosity, and particle size of PB, KB, and GG [37]. The high power density of PB can be owing to its conductive and porous nature, which allows more electron acceptors in the

anaerobic region and supports high exoelectrogenic biofilm formation [47,67]. Besides, CW-MFC with GG has depicted the lowest electrical performance despite high EC, and thus, PB can be deduced to be beneficial by virtue of its high surface area and porosity in comparison to GG [36]. Furthermore, CE of microcosms was found in the order of PB > KB > GG, through Eq. (2). The obtained CE values are low, which is consistent with other studies in CW-MFC field [11,68]. Although, relatively high CE % in PB microcosm may be owing to the domination of exoelectrogens rather than fermentative bacteria and other competing microbial processes such as methanogenesis, sulfate reduction in the system, and low production of intermediates and by-products such as hydrogen and formate [69]. Generally, CE is found to be low in CW-MFC systems due to the transfer of electrons through solution rather than external circuit and numerous other bio-electrochemical reactions [70]. Furthermore, several studies have reported improved power density and CE with biochar amendment on anode electrodes in microbial fuel cells [36,37,71].

3.6. Chemical oxygen demand removal

Average COD removal of 59.91 ± 3.21 %, 72.32 ± 2.98 %, and 72.42 ± 2.61 % were observed for PB, GG, and KB microcosm for the entire duration of operation with influent COD of 297.73 ± 9.59 mg L^{-1}. In CW-MFCs, COD removal is basically a consequence of diverse microbial metabolisms, which mainly involves exoelectrogenesis, fermentation, and methanogenesis [53]. In Fig. 5 (d), for PB microcosm, an unexpected drop in the removal of COD observed almost after four months of operation (*i.e.,* after the 25th sampling point). Before the 25th sampling point, average COD removal in PB microcosm was noted as 77.62 ± 3.34 %, which further decreased to 48.37 ± 3.13 %. This is in accordance with the ORP data, wherein a decrease in the cathodic ORP was observed after 4 months of PB operation. Also, weakened proton reduction reactions in CV voltammogram of PB after 6 months is inferring towards reduced glucose oxidation. Whereas, in case of KB, in the initial phase, a slow increase in COD removal with time was observed which can be explained by the time required by microbes for adaptability in the KB. This inference was further explained with gradually decreasing anodic ORP value with an increase in operation time of KB microcosm [72]. In a previous study, 17 % higher COD removal has been reported with biochar electrodes in comparison to stainless steel electrodes due to their biofilm-friendly nature relating to high porosity [13,36]. Besides, GG and KB showed an almost equal percentage of COD removal despite the high EC by GG. It may be further explained since different adsorptive removal of COD causing compounds by GG and KB materials.

3.7. Ammonium removal

The average ammonium removal of 22.65 ± 1.55 %, 17.13 ± 1.49 %, 16.29 ± 1.51 % was achieved in PB, GG, and KB microcosms, respectively, as shown in Fig. 5 (e). Ammonium removal is dependent on the availability of electron acceptors; however, low DO concentrations in the lower region of all microcosms indicate relative anaerobic conditions in the lower region of the microcosm. High DO diffusivity was noted in the upper region of PB and KB microcosms, but in this case, since the highest DO diffusion was in the KB microcosm, it implies there should also be higher ammonium removal, but our results differ from this notion. This could be due to the unavailability of wastewater up to the level of oxygen diffusion owing to the high-water holding capacity of KB (as discussed in the previous section). Thus, this rules out the ammonium treatment in the upper region of KB, implying the lower region of the microcosm is responsible for ammonium removal. In the anaerobic region, conductive material could act as electron acceptor and facilitates electron transfer to anode and from there, electrons flow to cathode and get reduced [49,70]. On the other hand, low water holding capacity and high oxygen diffusion in PB lead to high ammonium removal. Furthermore, internal resistance could also have played a crucial role in the ammonium removal process. It seems that internal resistance generally consists of charge transfer resistance (R_{ct}) and solution resistance (Rs), since GG and KB microcosms has a high internal resistance, suggesting high R_{ct} and R_s and thus limiting the electron transfer to the anode and slowing down the whole process of reduction at cathode [73]. Higher charge transfer resistance causes electron build-up in the anodic region, thus showing less ammonium removal efficiency in comparison to PB [70]. In Fig. 5 (e), high removal efficiency can be observed till the initial three sampling points in all the microcosms, which could be due to physical adsorption at the surfaces (detailed in *sec* 3.1).

3.8. Nitrate removal

The average nitrate removal in PB, GG, and KB microcosm were 98.02 ± 0.25 %, 97.86 ± 0.22 %, and 96 ± 0.44 %, respectively, with an initial nitrate concentration of 24.99 ± 0.78 mg L^{-1} as shown in Fig. 5 (f). High nitrate loading in the cathodic region could also enhance electricity generation by being utilized as an electron acceptor when oxygen availability is limited [74]. In our case, all the microcosms show > 95 % of nitrate removal, which is in agreement with low DO levels, thus maintaining preferable anaerobic conditions in the anodic region for nitrate removal [75]. Slightly higher nitrate removal in PB in comparison to other microcosms can be due to low internal resistance of the microcosm over KB and GG microcosms. Several studies have reported improved nitrate removal efficiency with lowered internal resistance owing to efficient electron utilization and thus also improving current generation [76,77].

4. Conclusions

The current study demonstrates a circular route of plant biomass utilization, generated in constructed wetland. The demonstrated process of electroactive biochar generation and their application in developing electroactive constructed wetlands provides a sustainable process of upgrading treatment and electricity generation performance of constructed wetlands. Produced *Canna indica* biomass based biochars differ in their physico-(electro)chemical properties based on the preparation method used. Plasma process-based processes produce biochar within few minutes that resulted in more crystalline biochar with high electrical conductivity compared to the amorphous material produced by using kiln method. These properties facilitated high electricity generation and microbial colonization and thus enhancing pollutants removal efficiencies and electricity generation efficiency. The present study could be further investigated in terms of influenced microbial diversity due to the application of diverse biochars. Microcosm designing could be further explored in terms of the addition of different vegetation, large-scale implementations, and workable energy harvesting aspects.

Further, the used biochar in different microcosms can be explored for utilizing as a soil conditioner and/or fertilizer for agricultural purposes owing to its various beneficial properties.

Declaration of Competing Interest

The authors declare that they have no known competing financial interests or personal relationships that could have appeared to influence the work reported in this paper.

Data availability

The authors do not have permission to share data.

Acknowledgements

Yamini Mittal acknowledges the GATE-SRF fellowship provided by

the Council of Scientific and Industrial Research (CSIR), India. She is also thankful to AcSIR, New Delhi, for helping her to carry out Ph.D. research work. Asheesh Kumar Yadav is grateful to CSIR-IMMT for providing all the facilities, infrastructure and CSIR India for sanctioning grant numbers MLP-037 and MLP-059, DST India for sanctioning the grant number DST/TMD-EWO/WTI/2K19/EWFH/2019/109 (GAP-340)] to carry out this research work. Asheesh Kumar Yadav and Fernando Martinez acknowledge the European Union H2020 research and innovation program (grant agreement number 754382) under Got Energy Talent Marie Curie Actions Fellowship. Manish Kumar acknowledges funding under joint project awarded by DST India [Grant number DST/TDT/WM/2019/5 (G)]. Authors are also grateful to Prof. Paul Anderson for providing technical training and guidance regarding rotatory kiln manufacturing and working.

Appendix A. Supplementary data

Supplementary data to this article can be found online at https://doi.org/10.1016/j.cej.2022.138587.

References

[1] P. Srivastava, Y. Mittal, S. Gupta, R. Abbassi, V. Garaniya, Recent progress in biosensors for wastewater monitoring and surveillance, Artif. Intell. Data Sci. Environ. Sens. (2022) 245–267.
[2] S. Gupta, P. Srivastava, S.A. Patil, A.K. Yadav, A comprehensive review on emerging constructed wetland coupled microbial fuel cell technology: potential applications and challenges, Bioresour. Technol. 320 (2021), 124376.
[3] P. Srivastava, A.K. Yadav, V. Garaniya, R. Abbassi, Chapter 6.3 - Constructed Wetland Coupled Microbial Fuel Cell Technology: Development and Potential Applications, in: S.V. Mohan, S. Varjani, A. Pandey (Eds.), Microb. Electrochem. Technol., Elsevier, 2019: pp. 1021–1036. https://doi.org/10.1016/B978-0-444-64052-9.00042-X.
[4] D. D'Amato, S. Veijonaho, A. Toppinen, Towards sustainability? Forest-based circular bioeconomy business models in Finnish SMEs, For.-Based Circ, Bioeconomy Matching Sustain. Chall. New Bus. Oppor. 110 (2020), 101848, https://doi.org/10.1016/j.forpol.2018.12.004.
[5] S. Gupta, Y. Mittal, R. Panja, K.B. Prajapati, A.K. Yadav, Conventional wastewater treatment technologies. Current Developments in Biotechnology and Bioengineering, Elsevier, 2021, pp. 47–75.
[6] P. Srivastava, S. Gupta, Y. Mittal, N.K. Dhal, T. Saeed, F. Martinez, A.K. Yadav, Constructed wetlands and its coupling with other technologies from lab to field scale for enhanced wastewater treatment and resource recovery. Novel Approaches Towards Wastewater Treatment and Resource Recovery Technologies, 419, 446, 2022.
[7] F. Masi, A. Rizzo, M. Regelsberger, The role of constructed wetlands in a new circular economy, resource oriented, and ecosystem services paradigm, J. Environ. Manage. 216 (2018) 275–284.
[8] A. Yadav, Design and development of novel constructed wetland cum microbial fuel cell for electricity production and wastewater treatment, in (2010) 4–10.
[9] P. Srivastava, R. Abbassi, A.K. Yadav, V. Garaniya, M. Asadnia, A review on the contribution of electron flow in electroactive wetlands: Electricity generation and enhanced wastewater treatment. Chemosphere 254 (2020) 126926.
[10] S. Gupta, Y. Mittal, P. Tamta, P. Srivastava, A.K. Yadav, Textile wastewater treatment using microbial fuel cell and coupled technology: a green approach for detoxification and bioelectricity generation, in, Integr. Microb. Fuel Cells Wastewater Treat., Elsevier (2020) 73–92.
[11] L. Doherty, Y. Zhao, X. Zhao, Y. Hu, X. Hao, L. Xu, R. Liu, A review of a recently emerged technology: constructed wetland–microbial fuel cells, Water Res. 85 (2015) 38–45.
[12] S. Chen, A.-E. Rotaru, P.M. Shrestha, N.S. Malvankar, F. Liu, W. Fan, K.P. Nevin, D. R. Lovley, Promoting interspecies electron transfer with biochar, Sci. Rep. 4 (2014) 1–7.
[13] T.M. Huggins, A. Latorre, J.C. Biffinger, Z.J. Ren, Biochar based microbial fuel cell for enhanced wastewater treatment and nutrient recovery, Sustainability. 8 (2016) 169.
[14] J. Wang, X. Song, Y. Wang, J. Bai, H. Bai, D. Yan, Y. Cao, Y. Li, Z. Yu, G. Dong, Bioelectricity generation, contaminant removal and bacterial community distribution as affected by substrate material size and aquatic macrophyte in constructed wetland-microbial fuel cell, Bioresour. Technol. 245 (2017) 372–378, https://doi.org/10.1016/j.biortech.2017.08.191.
[15] L. Xu, B. Wang, X. Liu, W. Yu, Y. Zhao, Maximizing the energy harvest from a microbial fuel cell embedded in a constructed wetland, Appl. Energy. 214 (2018) 83–91.
[16] Y. Yang, Y. Zhao, C. Tang, L. Xu, D. Morgan, R. Liu, Role of macrophyte species in constructed wetland-microbial fuel cell for simultaneous wastewater treatment and bioenergy generation, Chem. Eng. J. 392 (2020), 123708, https://doi.org/10.1016/j.cej.2019.123708.
[17] C. Tang, Y. Zhao, C. Kang, Y. Yang, D. Morgan, L. Xu, Towards concurrent pollutants removal and high energy harvesting in a pilot-scale CW-MFC: Insight into the cathode conditions and electrodes connection, Chem. Eng. J. 373 (2019) 150–160.
[18] L. Xu, Y. Zhao, C. Fan, Z. Fan, F. Zhao, First study to explore the feasibility of applying microbial fuel cells into constructed wetlands for COD monitoring, Bioresour. Technol. 243 (2017) 846–854.
[19] Y. Yang, Y. Zhao, C. Tang, Y. Mao, T. Chen, Y. Hu, Novel pyrrhotite and alum sludge as substrates in a two-tiered constructed wetland-microbial fuel cell, J. Clean. Prod. 293 (2021), 126087.
[20] J. Wang, X. Song, Q. Li, H. Bai, C. Zhu, B. Weng, D. Yan, J. Bai, Bioenergy generation and degradation pathway of phenanthrene and anthracene in a constructed wetland-microbial fuel cell with an anode amended with nZVI, Water Res. 150 (2019) 340–348.
[21] K. Sonu, M. Sogani, Z. Syed, Integrated Constructed Wetland-Microbial Fuel Cell using Biochar as Wetland Matrix: Influence on Power Generation and Textile Wastewater Treatment, ChemistrySelect. 6 (2021) 8323–8328.
[22] S. Singh, B. Mohanty, S. Basu, Synthesis of SiC from rice husk in a plasma reactor, Bull. Mater. Sci. 25 (2002) 561–563.
[23] Paul S Anderson, RoCC Kiln Manual: (version 2020-03-27), Rotatable Covered Cavity Kilns for Pyrolytic Production of Biochar for Sequestration and Woodgas for Energy (BC&E), Woodgas Pyrolytics, Inc. 227 South Orr Drive Normal, Illinois 61761 USA, (2020). https://woodgas.com/wpcontent/uploads/2020/03/RoCC-kiln-Manual-2020-03-27.pdf.
[24] Y. Yang, Y. Zhao, C. Tang, Y. Mao, C. Shen, Significance of water level in affecting cathode potential in electro-wetland, Bioresour. Technol. 285 (2019), 121345.
[25] J. Villasenor, P. Capilla, M. Rodrigo, P. Canizares, F. Fernandez, Operation of a horizontal subsurface flow constructed wetland–microbial fuel cell treating wastewater under different organic loading rates, Water Res. 47 (2013) 6731–6738.
[26] A.P.H. Association, APHA (2005) Standard methods for the examination of water and wastewater, APHA Wash, DC USA, 2005.
[27] H. Liu, S. Cheng, B.E. Logan, Power generation in fed-batch microbial fuel cells as a function of ionic strength, temperature, and reactor configuration, Environ. Sci. Technol. 39 (2005) 5488–5493.
[28] Z. He, F. Mansfeld, Exploring the use of electrochemical impedance spectroscopy (EIS) in microbial fuel cell studies, Energy Environ. Sci. 2 (2009) 215–219.
[29] A. Enders, K. Hanley, T. Whitman, S. Joseph, J. Lehmann, Characterization of biochars to evaluate recalcitrance and agronomic performance, Bioresour. Technol. 114 (2012) 644–653.
[30] L. Goswami, N.A. Manikandan, J.C.R. Taube, K. Pakshirajan, G. Pugazhenthi, Novel waste-derived biochar from biomass gasification effluent: preparation, characterization, cost estimation, and application in polycyclic aromatic hydrocarbon biodegradation and lipid accumulation by Rhodococcus opacus, Environ. Sci. Pollut. Res. 26 (2019) 25154–25166.
[31] A.I. Ferjani, M. Jeguirim, S. Jellali, L. Limousy, C. Courson, H. Akrout, N. Thevenin, L. Ruidavets, A. Muller, S. Bennici, The use of exhausted grape marc to produce biofuels and biofertilizers: Effect of pyrolysis temperatures on biochars properties, Renew. Sustain. Energy Rev. 107 (2019) 425–433.
[32] M. Pimenta, G. Dresselhaus, M.S. Dresselhaus, L. Cancado, A. Jorio, R. Saito, Studying disorder in graphite-based systems by Raman spectroscopy, Phys. Chem. Chem. Phys. 9 (2007) 1276–1290.
[33] A.K. Kercher, D.C. Nagle, Evaluation of carbonized medium-density fiberboard for electrical applications, Carbon. 40 (2002) 1321–1330.
[34] T. Sun, B.D. Levin, J.J. Guzman, A. Enders, D.A. Muller, L.T. Angenent, J. Lehmann, Rapid electron transfer by the carbon matrix in natural pyrogenic carbon, Nat. Commun. 8 (2017) 1–12.
[35] A.M. Bagoji, S.T. Nandibewoor, Electrocatalytic redox behavior of graphene films towards acebutolol hydrochloride determination in real samples, New J. Chem. 40 (2016) 3763–3772.
[36] C.-T. Wang, T. Sangeetha, D.-Q. Ding, W.-T. Chong, W.-M. Yan, Implementation of surface modified carbon cloth electrodes with biochar particles in microbial fuel cells, Int. J. Green Energy. 15 (2018) 789–794.
[37] T. Huggins, H. Wang, J. Kearns, P. Jenkins, Z.J. Ren, Biochar as a sustainable electrode material for electricity production in microbial fuel cells, Bioresour. Technol. 157 (2014) 114–119.
[38] C. Pituello, O. Francioso, G. Simonetti, A. Pisi, A. Torreggiani, A. Berti, F. Morari, Characterization of chemical–physical, structural and morphological properties of biochars from biowastes produced at different temperatures, J. Soils Sediments. 15 (2015) 792–804.
[39] X. Cui, S. Fang, Y. Yao, T. Li, Q. Ni, X. Yang, Z. He, Potential mechanisms of cadmium removal from aqueous solution by Canna indica derived biochar, Sci. Total Environ. 562 (2016) 517–525.
[40] C. Takaya, L. Fletcher, S. Singh, K. Anyikude, A. Ross, Phosphate and ammonium sorption capacity of biochar and hydrochar from different wastes, Chemosphere. 145 (2016) 518–527.
[41] A.A. Karim, M. Kumar, S.K. Singh, C.R. Panda, B.K. Mishra, Potassium enriched biochar production by thermal plasma processing of banana peduncle for soil application, J. Anal. Appl. Pyrolysis. 123 (2017) 165–172.
[42] P. Trazzi, J.J. Leahy, M.H. Hayes, W. Kwapinski, Adsorption and desorption of phosphate on biochars, J. Environ. Chem. Eng. 4 (2016) 37–46.
[43] V. Ţucureanu, A. Matei, A.M. Avram, FTIR spectroscopy for carbon family study, Crit. Rev. Anal. Chem. 46 (2016) 502–520.
[44] Z. Wang, H. Guo, F. Shen, G. Yang, Y. Zhang, Y. Zeng, L. Wang, H. Xiao, S. Deng, Biochar produced from oak sawdust by Lanthanum (La)-involved pyrolysis for

adsorption of ammonium (NH4+), nitrate (NO3−), and phosphate (PO43−), Chemosphere. 119 (2015) 646–653.
[45] W. Zheng, B. Sharma, N. Rajagopalan, Using biochar as a soil amendment for sustainable agriculture, Waste Util.–Biochar. (2010).
[46] I. Chakraborty, S. Sathe, B. Dubey, M. Ghangrekar, Waste-derived biochar: Applications and future perspective in microbial fuel cells, Bioresour. Technol. 312 (2020), 123587.
[47] D. Cheng, H.H. Ngo, W. Guo, S.W. Chang, D.D. Nguyen, J. Li, Q.V. Ly, T.A. H. Nguyen, Applying a new pomelo peel derived biochar in microbial fell cell for enhancing sulfonamide antibiotics removal in swine wastewater, Bioresour. Technol. 318 (2020), 123886.
[48] Y.-L. Oon, S.-A. Ong, L.-N. Ho, Y.-S. Wong, Y.-S. Oon, H.K. Lehl, W.-E. Thung, Hybrid system up-flow constructed wetland integrated with microbial fuel cell for simultaneous wastewater treatment and electricity generation, Bioresour. Technol. 186 (2015) 270–275.
[49] P. Srivastava, A.K. Yadav, B.K. Mishra, The effects of microbial fuel cell integration into constructed wetland on the performance of constructed wetland, Bioresour. Technol. 195 (2015) 223–230.
[50] P. Saket, Y. Mittal, K. Bala, A. Joshi, A. Kumar Yadav, Innovative constructed wetland coupled microbial fuel cell for enhancing diazo dye degradation with simultaneous electricity generation, Bioresour. Technol. (2021), 126490, https://doi.org/10.1016/j.biortech.2021.126490.
[51] Y. Mittal, S. Dash, P. Srivastava, P.M. Mishra, T.M. Aminabhavi, A.K. Yadav, Azo dye containing wastewater treatment in earthen membrane based unplanted two chambered constructed wetlands-microbial fuel cells: A new design for enhanced performance, Chem. Eng. J. 427 (2022), 131856.
[52] P. Srivastava, R. Abbassi, V. Garaniya, T. Lewis, A.K. Yadav, Performance of pilot-scale horizontal subsurface flow constructed wetland coupled with a microbial fuel cell for treating wastewater, J. Water Process Eng. 33 (2020), 100994.
[53] L. Zhuang, S. Zhou, Y. Li, Y. Yuan, Enhanced performance of air-cathode two-chamber microbial fuel cells with high-pH anode and low-pH cathode, Bioresour. Technol. 101 (2010) 3514–3519.
[54] J.C. Biffinger, J. Pietron, O. Bretschger, L.J. Nadeau, G.R. Johnson, C.C. Williams, K.H. Nealson, B.R. Ringeisen, The influence of acidity on microbial fuel cells containing Shewanella oneidensis, Biosens. Bioelectron. 24 (2008) 900–905.
[55] M. Ahmad, A.U. Rajapaksha, J.E. Lim, M. Zhang, N. Bolan, D. Mohan, M. Vithanage, S.S. Lee, Y.S. Ok, Biochar as a sorbent for contaminant management in soil and water: a review, Chemosphere. 99 (2014) 19–33.
[56] B.-Y. Geng, L.-Y. Cao, F. Li, H. Song, C.-G. Liu, X.-Q. Zhao, F.-W. Bai, Potential of Zymomonas mobilis as an electricity producer in ethanol production, Biotechnol. Biofuels. 13 (2020) 1–11.
[57] A. Downie, A. Crosky, P. Munroe, Physical properties of biochar, Biochar Environ. Manag, Sci. Technol. 1 (2009).
[58] M. Kumar, R. Gupta, Electrical resistivity of Acacia and Eucalyptus wood chars, J. Mater. Sci. 28 (1993) 440–444.
[59] L. Yu, Y. Wang, Y. Yuan, J. Tang, S. Zhou, Biochar as electron acceptor for microbial extracellular respiration, Geomicrobiol. J. 33 (2016) 530–536.
[60] X. Cai, Y. Yuan, L. Yu, B. Zhang, J. Li, T. Liu, Z. Yu, S. Zhou, Biochar enhances bioelectrochemical remediation of pentachlorophenol-contaminated soils via long-distance electron transfer, J. Hazard. Mater. 391 (2020), 122213.
[61] G. Mohanakrishna, S.V. Mohan, P. Sarma, Utilizing acid-rich effluents of fermentative hydrogen production process as substrate for harnessing bioelectricity: an integrative approach, Int. J. Hydrog. Energy. 35 (2010) 3440–3449.
[62] S.V. Mohan, S. Srikanth, P. Sarma, Non-catalyzed microbial fuel cell (MFC) with open air cathode for bioelectricity generation during acidogenic wastewater treatment, Bioelectrochemistry. 75 (2009) 130–135.
[63] S.V. Raghavulu, S.V. Mohan, M.V. Reddy, G. Mohanakrishna, P. Sarma, Behavior of single chambered mediatorless microbial fuel cell (MFC) at acidophilic, neutral and alkaline microenvironments during chemical wastewater treatment, Int. J. Hydrog. Energy. 34 (2009) 7547–7554.
[64] D.A. Jadhav, M.M. Ghangrekar, Effective ammonium removal by anaerobic oxidation in microbial fuel cells, Environ. Technol. 36 (2015) 767–775.
[65] Y.-C. Yong, Y.-Y. Yu, Y. Yang, C.M. Li, R. Jiang, X. Wang, J.-Y. Wang, H. Song, Increasing intracellular releasable electrons dramatically enhances bioelectricity output in microbial fuel cells, Electrochem. Commun. 19 (2012) 13–16.
[66] K.P. Katuri, P. Kavanagh, S. Rengaraj, D. Leech, Geobacter sulfurreducens biofilms developed under different growth conditions on glassy carbon electrodes: insights using cyclic voltammetry, Chem. Commun. 46 (2010) 4758–4760.
[67] C.S. Ayyappan, V. Bhalambaal, S. Kumar, Effect of biochar on bio-electrochemical dye degradation and energy production, Bioresour. Technol. 251 (2018) 165–170.
[68] A. Ebrahimi, M. Sivakumar, C. McLauchlan, A. Ansari, A. Vishwanathan, A critical review of the symbiotic relationship between constructed wetland and microbial fuel cell for enhancing pollutant removal and energy generation, J. Environ. Chem. Eng. 9 (2021), 105011.
[69] A. Ter Heijne, M. Pereira, J. Pereira, T. Sleutels, Electron storage in electroactive biofilms, Trends Biotechnol (2020).
[70] P. Srivastava, A.K. Yadav, V. Garaniya, T. Lewis, R. Abbassi, S.J. Khan, Electrode dependent anaerobic ammonium oxidation in microbial fuel cell integrated hybrid constructed wetlands: A new process, Sci. Total Environ. 698 (2020), 134248.
[71] F. Xu, D. Ouyang, E.R. Rene, H.Y. Ng, L. Guo, Y. Zhu, L. Zhou, Q. Yuan, M. Miao, Q. Wang, Electricity production enhancement in a constructed wetland-microbial fuel cell system for treating saline wastewater, Bioresour. Technol. 288 (2019), 121462.
[72] X. Wang, Y. Feng, N. Ren, H. Wang, H. Lee, N. Li, Q. Zhao, Accelerated start-up of two-chambered microbial fuel cells: effect of anodic positive poised potential, Electrochimica Acta. 54 (2009) 1109–1114.
[73] X. Li, X. Wang, Q. Zhao, L. Wan, Y. Li, Q. Zhou, Carbon fiber enhanced bioelectricity generation in soil microbial fuel cells, Biosens. Bioelectron. 85 (2016) 135–141.
[74] L. Doherty, Y. Zhao, X. Zhao, W. Wang, Nutrient and organics removal from swine slurry with simultaneous electricity generation in an alum sludge-based constructed wetland incorporating microbial fuel cell technology, Chem. Eng. J. 266 (2015) 74–81.
[75] S. Gupta, A. Nayak, C. Roy, A.K. Yadav, An algal assisted constructed wetland-microbial fuel cell integrated with sand filter for efficient wastewater treatment and electricity production, Chemosphere. 263 (2021), 128132.
[76] J.-T. Li, S.-H. Zhang, Y.-M. Hua, Performance of denitrifying microbial fuel cell subjected to variation in pH, COD concentration and external resistance, Water Sci. Technol. 68 (2013) 250–256.
[77] P. Tamta, N. Rani, A.K. Yadav, Enhanced wastewater treatment and electricity generation using stacked constructed wetland–microbial fuel cells, Environ. Chem. Lett. 1–9 (2020).